Thermal modeling of DED repair process for slender panels by a 2D semi-analytic approach

Camille Guévenoux, Mohamad Nasiry, Sylvain Durbecq, Alexandre Charles, Eric Charkaluk, Andrei Constantinescu

Thermal modeling of DED repair process for slender panels by a 2D semi-analytic approach

Camille Guévenoux[a,b], Mohamad Nasiry[a], Sylvain Durbecq[a], Alexandre Charles[b], Eric Charkaluk[a], Andrei Constantinescu[a]

[a] *Laboratoire de Mécanique des Solides, École polytechnique, Institut Polytechnique de Paris, CNRS, Palaiseau, France*
[b] *Safran Tech, Magny-les-Hameaux, France*

Abstract

Directed Energy Deposition is one of the leading additive manufacturing technologies tailored for the repair of metallic components. The spatial and temporal pattern of the heat flux results in specific thermal gradients and cooling rates, controlling the final microstructure and mechanical properties of the repaired component. Simplified thermal analyses based on Rosenthal's solution offers an interesting way to model in short computational times the repair process of simple geometries, estimating the spatial thermal gradients or cooling rates. This article presents a new model based on Rosenthal's solution. Compared to other existing analytic solutions, the present work contains material layer addition and therefore enables the modeling of not only one layer but of the complete additive manufacturing process. The validity domain of the model is identified using experimental measurements on 316L stainless steel. Possible applications are also provided: determination of solidification regime (columnar or equiaxed grains) in solidification maps or optimization of the duration of interlayer dwell time needed to keep the part under a low annealing temperature.

Keywords: Directed Energy Deposition, slender panel repair, analytic thermal modeling.

Contents

1 Introduction **2**

2 Material and methods **3**
2.1 Geometry and process parameters . . . 3
2.2 Thermal instrumentation . . . 3

3 Model description **4**
3.1 Solution of the transient heat equation on a semi-infinite panel . . . 5
3.2 Modeling the edges of a finite panel . . . 6
3.3 Spatial extension of sources . . . 6
3.4 Printing successive layers . . . 7
3.5 Numerical implementation and computational time . . . 8

4 Results **8**
4.1 Parameter identification from thermocouples measurements . . . 8
4.2 Model validation on thermal camera data . . . 10
4.3 Limits of superposition principle . . . 11
4.4 Conclusions . . . 12

5 Discussion **12**
5.1 Validity domain . . . 12
5.2 Three-dimensional structures . . . 15
5.3 Determination of optimal dwell time . . . 15
5.4 Spatial thermal gradient and solidification maps . . . 15

Email address: camille.guevenoux@polytechnique.edu (Camille Guévenoux)

6 Conclusion **17**

7 Appendices **20**
7.1 Appendix 1: Fast integration model of the transient heat equation 20
7.2 Appendix 2: From transient to steady solution 22
7.3 Appendix 3: Position of fictitious sources 23

1. Introduction

The manufacturing process of a component defines not only its shape but also, through thermal gradients and cooling rates, its microstructure which drives its final mechanical behavior. Additive manufacturing, and in particular Directed Energy Deposition (DED), is a key technology offering new opportunities to repair complex components. The thermal history endured by the part during this process is very different from conventional processes like forge or foundry. Indeed, because of the localized energy input, the part is submitted to pronounced spatial thermal gradient and to fast cooling rates which are fully controlled by the various process parameters whose influence have been thoroughly studied in the literature. Among others, let us mention the main process parameters driving those specific solidification conditions: laser speed, laser power and powder flow rate [1–3], linear energy input (laser power divided by laser speed) [4, 5], lasing strategy [3, 6–9] and inter-layer dwell time [10–12]. Due to the large numbers of significant parameters, simulating the thermal field during additive manufacturing is crucial to gain information about the solidification conditions and consequently about final microstructure and properties.

High-fidelity Finite Element simulations enable to describe accurately the solidification phenomenon [13] and yet, due to memory and time constraints, a compromise needs to be found between the size of the studied domain and the amount of physics phenomenon modeled: some simulations focuses on the melt pool scale [14, 15], others model the building of a few layers [16, 17], while other authors chose to neglect small scale phenomenon to model the manufacturing of the whole component [11, 18, 19]. Indeed, as highlighted by Veldman *et al.* in [20], several numerical challenges arise using Finite Element Analysis for such problems: material addition, mesh refinement at the laser spot, modeling of phase changes, etc. Consequently, high-fidelity simulations are too heavy to be used at the component level, in a development phase, where different set of process parameters need to be investigated.

This is why, for preliminary studies on simplified geometries, it is very appealing to consider faster models based on analytic solutions. Carslaw in 1921 [21], followed by Rosenthal in 1946 [22] developed analytic expressions of the thermal increment caused by a local heat source. Following these works, a large number of extensions were carried out to model welding [23–29]. With the increase of computational capacities, analytic methods have lost ground in favor of numerical methods but recently the effort to study additive manufacturing process with large size models has brought Rosenthal's solution up to date [13]. Gockel et al. proposed [30] to use such quasi-steady Rosenthal's solution to investigate the influence of free edges on the melt pool shape and solidification conditions for one laser path. Promoppatum *et al.* [31] and Yang *et al.* [32] used similar analytic or semi-analytic models for Selective Laser Melting, whereas Parkitny and Winczek developed an analytic solution modeling the impact of tilting the heat source [33]. Those solutions offer the advantage to give good estimations of thermal field in short computation times. However, they only enables the computation of temperature during the manufacturing of one layer process since none of them contains material addition.

The motivation of this work is to study the repair with DED of damaged slender panels (see [34, 35] for similar geometries and [36, 37] for applications). To do so, the issue of material addition is addressed and an extension of Rosenthal's solution is applied to the modeling of DED repair process with several laser paths. The major aspects of the present model are the following; first, the thermal field is derived in the transient regime, taking into account the effect of cooling due to conduction; then, convection loss is added to the thermal solution; finally the temperature increments caused by the printing of several layers are summed. This final step is done using the superposition principle and can consequently only been done for thermal linear cases. To ensure the validity of this hypothesis, additional dwell times were then added between the printing of the layers to cool down the manufactured component. The specificity of this model compared to other works of the literature is highlighted in Tab. 1.

The present paper starts by a presentation of the experimental set-up in Sect. 2. A description of the model is then given in Sect. 3. Below, in Sect. 4, a comparison between experimental measurements and model predictions is made to calibrate it and to define its validity domain. Finally, in Sect.5, discussions on potential improvements as well as possible applications are provided.

		Time	
		Numerical Finite Differences	Analytic
Space	Numerical FEM	• high-fidelity models limited to small volumes [14, 15] • low-fidelity models at component scale [11, 18]	$\emptyset$
	Analytic	**• present model: simplified geometry, convection, addition of material**	• Rosenthal's solution [29–32]

Table 1: Main features of existing models for thermal simulation of the additive manufacturing process: comparison of literature with present work.

2. Material and methods

2.1. Geometry and process parameters

The configuration investigated here is similar to a repaired slender part and consists in depositing by DED a single-track wall on top of a thin wrought plate, referred to as substrate. The coordinate system used in all the present paper is defined as follows: the $x = 0$ plane correspond to the left edge of the single-track wall and the $z = 0$ plane is at the interface between the substrate and the printed part. This geometry and coordinate system is described in Fig. 1b

The substrate is a 316L stainless steel (SS316) plate. The material deposited is an industrial SS316 powder with sieve range $45 - 105\,\mu m$, provided by *Oerlikon* [38].

The samples were manufactured with a *BeAM Mobile* machine (see [39] for additional details on the manufacturer). This machine is equipped with a coaxial nozzle (*10Vx* nozzle) including a powder jet, a local argon inerting and a fiber laser with wavelength $1070\,nm$ offering a maximum power of $500\,W$ and a spot diameter of $0.75\,mm$.

The process parameters were kept identical for all samples: laser speed ($2000\,mm/min = 33.3\,mm/s$), laser power ($250\,W$), powder mass flow (from 6.5 to $7\,g/min$), vertical increment between two layers ($0.2\,mm$). The deposition strategy is a back and forth straight movement of the nozzle. Two types of lasing conditions were applied:

(a) standard continuous deposition, without any dwell time;
(b) deposition with a 30-second dwell time between two successive layers.

The duration of the dwell time can be compared to the classical duration of one laser path. The length of the manufactured wall is $100\,mm$ so with a laser path of $2000\,mm/min$, it takes 3 seconds to print one layer, the dwell time was then chosen to be 10 times longer than one laser path.

2.2. Thermal instrumentation

The substrates have been instrumented with two thermocouples of type K, covering a measurement range, starting from ambient temperature to 1350°C [40]. Their acquisition frequency is 10 Hz. Due to this low sampling rate, they cannot capture the very fast thermal evolution occurring during DED (cooling rates $10^3 - 10^4\,K/s$ [41]) and therefore, they cannot be used to assess peak temperatures. The thermocouples were welded on two substrates at the positions indicated on Fig. 1b: T1 ($x = 50\,mm, z = 0\,mm$) and T2 ($x = 50\,mm, z = -5\,mm$). These substrates were then used to manufacture two specimen, respectively without dwell time or with a 30-second dwell time.

The manufacturing was also monitored using a thermal camera which provides the temperature directly on the additively manufactured wall. The thermal camera used in this study is a *Xi400* from *Optris* [42] with the following main technical characteristics : wavelength 7.5 to $13\,\mu m$; temperature range 150 to $900\,°C$; detector size 382 x 288 pixels; accuracy $\pm 2\,\%$. In the present configuration, the pixel size was $370\,\mu m$ and the acquisition frequency $27\,Hz$. The emissivity of DED 316L in the camera range of wavelength was calibrated experimentally up to $600\,°C$. It was observed that this emissivity is almost constant with temperature and is around 30%.

As described in Fig. 2, the data acquired with the thermal camera can be used in two different ways:

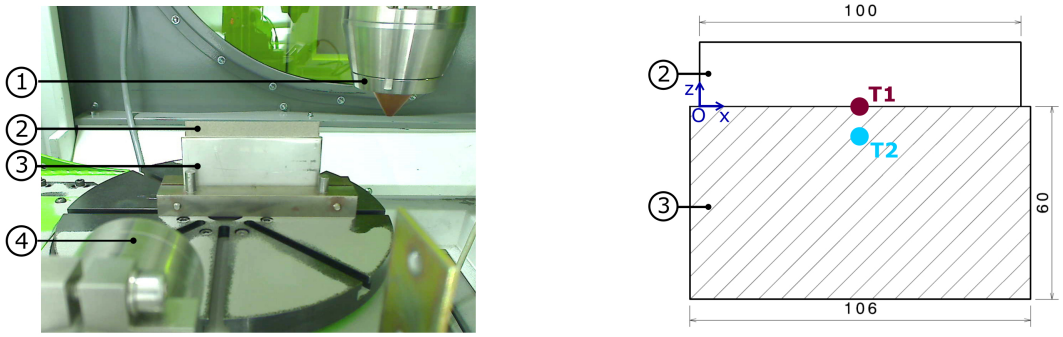

(a) Experimental set-up.

(b) Dimensions of specimen.

Figure 1: Thermal measurements during the additive manufacturing process of a repaired specimen: (a) instrumentation in the DED machine, 1) DED nozzle, 2) DED part, 3) Substrate, 4) Thermal camera; (b) position of thermocouples welded on the substrate.

(a) maps displaying the spatial distribution of temperature can be drawn at a given moment.
The maximum temperature of the camera being only $900\,°C$ and the pixel size being large compared to the melt pool size, the maximum temperature registered on those maps stands below the real peak temperature. However, far from the melt pool, the thermal camera enables to follow the tail following the heat source.

(b) time evolution can be derived at a certain position of the manufactured component using the values over time of the same pixel.
Due to experimental uncertainties and low sampling rate of the camera ($27\,Hz$) compared to the characteristic time of temperature evolution, this representation does not capture accurately the peak temperature. Nevertheless, the cooling rates and global tendencies above the camera minimum temperature $150\,°C$ are valuable information.

3. Model description

Geometry	a	Initial substrate height	60	mm
	L_{sub}	Substrate length	106	mm
	e	Wall thickness	0.8	mm
	L	Laser track length	100	mm
	n	Number of layers	40	-
Process	h	Convection coefficient	25	$\text{W.m}^{-2}\text{.K}^{-1}$
	v	Laser speed	2000	mm.min^{-1}
	Δz	Height of one layer	0.2	mm
	A	Absorptivity	0.35	-
	P	Laser power	250	W
	$Q = AP$	Absorbed power	87.5	W
Material	T_f	Melting temperature (liquidus)	1400	°C
	k	Thermal conductivity	16.3	$\text{W.m}^{-1}\text{.K}^{-1}$
	c	Specific heat capacity	500	$\text{J.kg}^{-1}\text{.K}^{-1}$
	ρ	Density	8000	kg.m^{-3}
	$D = 1/(2\lambda) = k/c\rho$	Thermal diffusivity	4.07e-06	$\text{m}^2\text{.s}^{-1}$

Table 2: Notations and values of model parameters. The material coefficients for 316L stainless steel are taken from [43].

The following assumptions are considered. The thickness e of the panel being negligible compared to its height a and width L_{sub}, it will be assumed that the temperature does not vary much along the

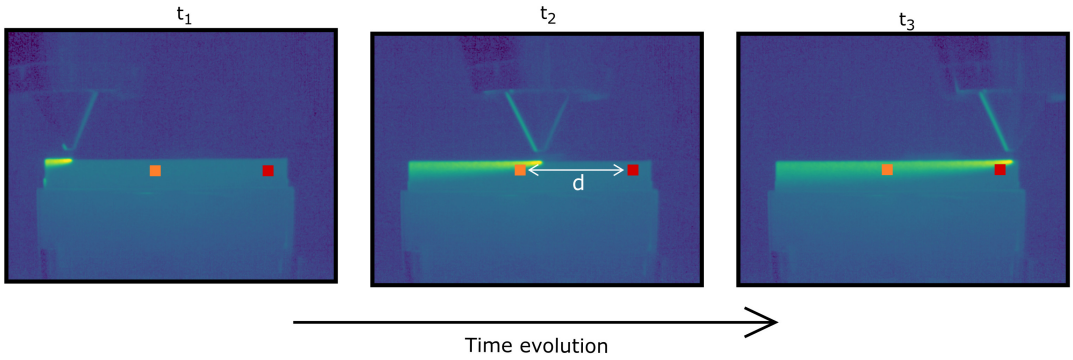

(a) Thermal fields at three different time instants during the manufacturing of a layer.

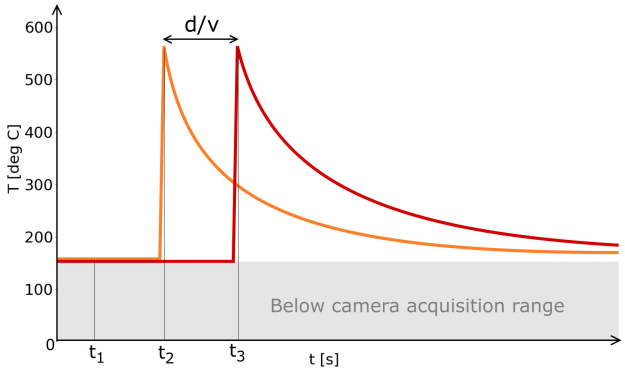

(b) Temporal evolution of temperature for two pixels separated by a distance d along the laser path.

Figure 2: The data acquired with the thermal camera can be displayed in two different ways: (a) spatial distributions at a given moment; (b) time evolution at certain position.

wall thickness (y direction) and calculations will be two-dimensional. The material parameters for 316L stainless steel were taken from [43] and are listed in Tab. 2. It is important to notice that the material coefficients are taken as constant and do not vary with temperature. This approximation is necessary to derive the analytic solution proposed in this study. In particular, this strong assumption prevents us from modeling phase change and will affect the accuracy of the model around the melt pool.

In order to explain how the model is built, the modeling of a single laser path is described first. The solution for the semi-infinite panel is given in Sect. 3.1, then the way to take into account the panel edges is explained in Sect. 3.2. Finally, the addition of material with the printing of the successive layers is tackled in Sect. 3.4. Only the main equations are presented in this paragraph, additional details on the method used to derive them can be found in the appendices, Sect. 7.1, 7.2 and 7.3.

3.1. Solution of the transient heat equation on a semi-infinite panel

In the absence of sources, the heat equation in 3D writes:

$$\frac{\partial T}{\partial t} - D\nabla^2 T = 0 \tag{1}$$

if $D = 1/(2\lambda) = k/c\rho$ the thermal diffusivity is assumed to be independent of temperature.

The thermal increment due to a heat source located at point (x', z') delivering an instantaneous power dQ/e at instant t' is considered. The Appendix 7.1 details explanations about the derivation of the system of equations, denoted $\mathcal{P}_c$, satisfied by the two-dimensional thermal field:

$$\text{Problem } \mathcal{P}_c \begin{cases} \dfrac{\partial^2 T}{\partial x^2} + \dfrac{\partial^2 T}{\partial z^2} - 2\lambda \dfrac{\partial T}{\partial t} & = & f, \\ T & \xrightarrow{t\to 0} & 0\ , \quad r > 0, \\ T & \xrightarrow{r\to\infty} & 0, \\ -\displaystyle\int_0^{t_0} \frac{\partial T}{\partial r}\, \pi r\, k\, dt & \xrightarrow[t_0\to 0]{r\to 0} & \dfrac{dQ}{e}, \end{cases} \tag{2}$$

where f is a source term which depends on thermal loss in the following way. In the case of an adiabatic panel, $f = 0$ and the first line of this system is simply the heat equation in 2D. However, if the convection along the two main edges of the structure ($y = 0$ and $y = e$) is accounted for, the 3D boundary condition of convection can be transformed in a source term in 2D and $f = \dfrac{2h}{ek}\,T$. This derivation is explicitly done in Appendix 7.1.

Rosenthal provides in [22] a solution to the previous system in adiabatic conditions when $f = 0$. An extension of this solution is proposed when $f = \dfrac{2h}{ek}\,T$. The transient solution corresponding to the infinitesimal thermal increment caused by a source delivering dQ/e at point (x', z') at instant t' writes:

$$dT(x,z,t) = \frac{Q}{2\pi k e}\,\exp\left[-\frac{\lambda\left((x-vt')^2+(z-z')^2\right)}{2(t-t')} - \frac{2h(t-t')}{ec\rho}\right]\,\frac{dt'}{t-t'} \tag{3}$$

From this infinitesimal thermal increment, the total elevation of temperature can easily be derived by integrating the contributions of infinitesimal sources along the laser path.

$$T(x,z,t) = \int_{t'=0}^{t} dT(x,z,t) \tag{4}$$

Consequently, this simple semi-analytic expression gives the transient thermal field in a semi-infinite panel submitted to one laser path and to convection along its two main edges.

3.2. Modeling the edges of a finite panel

The previous section 3.1 exhibits the derivation of the thermal increment for a semi-infinite panel. However, in many applications, the edges are not far enough from the laser spot to be neglected, it is then necessary to model the edges.

In [22], Rosenthal makes the equivalence between an adiabatic edge and a plane of symmetry (in both case, no thermal flux crosses the surface) and offers to model the edges of the structure using image sources. The same method is used by Tan *et al.* in [44] and by Gockel *et al.* in [30] to take into account lateral edges. In a more general way, Yang *et al.* described in [32] a method to integrate any edge of a structure as soon as its surface is convex.

In the present configuration, four edges have to be modeled: the top and bottom edges $z = 0$ and $z = -a$ and the left and right edges $x = 0$ and $x = L$. Theoretically, an infinite number of sources should be added to ensure that the edges are planes of symmetry. Nevertheless, it is possible to demonstrate that at the first order (cf. appendix 7.3), only the closest sources plays a significant part in the thermal field. The majority of them are then neglected and only the closest to the real structure are taken into account. The appendix 7.3 explains in detail how those fictitious sources moves following the nozzle motion.

3.3. Spatial extension of sources

All the equations above deal with a punctual heat source in two dimensions, that is to say a linear heat source in three dimensions. Heat sources can also be described with a spatial extension accounting for the laser spot size. In this case, the power delivered by the source is a function of space $Q(u)$. The total temperature increment Eq. 29 for a punctual heat source need to be revised by integrating along u the contributions of all infinitesimal punctual sources composing the surface source:

$$T(x,z,t) = \int_{t'=0}^{t}\int_{u=-\infty}^{+\infty} \frac{Q(u)\;du}{2\pi\;k\;e}\,\exp\left[-\frac{\lambda\left((x-vt'+u)^2+(z-z')^2\right)}{2(t-t')} - \frac{2h(t-t')}{ec\rho}\right]\,\frac{dt'}{t-t'}. \tag{5}$$

For example, for a uniform surface heat source,

$$Q(u) = \begin{cases} Q/l & \text{if } -l/2 \le u \le l/2\ , \\ 0 & \text{otherwise;} \end{cases} \tag{6}$$

or for semi-Gaussian heat source,

$$Q(u) = \frac{Q}{\sigma\sqrt{2\pi}}\,\exp\left(-\frac{u^2}{2\sigma^2}\right) \quad \text{with} \quad 3\,\sigma = \frac{l}{2}. \tag{7}$$

However, since the spatial distribution of the heat source is small with respect to the panel dimension (laser spot 0.75mm on the *BeAM* DED machine used in this study, cf. Sect. 2 for more details), the thermal field is only affected by this surface modeling of the heat source in a small region around the melt pool. Since in the model no phase change is taken into account, the prediction of temperature around the melt pool should not be considered as accurate. Besides, modeling a surface heat source increases computation times since a spatial integration is added the temporal integration as shown in Eq. 6 and 7. Consequently, it has been chosen to keep a point heat source as the goal of the present model is to have an evaluation of temperature field in the overall structure in a short computational time.

3.4. Printing successive layers

For now, the modeling of only a single laser track has been discussed. However, when component repair is considered, several layers are deposited on top of each other to rebuild the initial geometry with a final total height of $a_f = a + n\Delta z$ where Δz is the height of one layer and n is the number of layers. The additive manufacturing process is by essence continuous. Nevertheless, due to the analytic formulation of space integration, there is no choice but to discretize the material addition and to add a whole layer at once.

The deposition of each layer will be ensured by a source S_i, $i \in [1\ ;\ n]$, located at $z_i' = i\Delta z$ and moving along the top edge of the panel of height $a_i = a + i\Delta_z$ at constant speed v. If the laser goes always in the same direction $x_i' = v(t' - t_i)$ for all layers. If the laser changes direction between two successive layers (back and forth motion), when $i = 2k + 1$ the source moves at speed from $x' = 0$ to $x' = L$, ie $x' = v(t' - t_i)$; when $i = 2k$, the source goes to speed $-v$ from $x' = L$ to $x' = 0$, ie $x' = L - v(t' - t_i)$.

The printing of one layer takes a time L/v. An additional dwell time noted t_{dwell} can be added between the printing of successive layers. Then, in total the duration of one laser path is $\Delta t_{\text{path}} = L/v + t_{dwell}$ and the time at which the printing of layer i begins is $t_i = (i-1)\Delta t_{\text{path}}$. The source S_i consequently delivers a power:

$$Q_i(t') = \begin{cases} AP & \text{if } t_i \leq t' \leq t_i + L/v, \\ 0 & \text{otherwise.} \end{cases} \tag{8}$$

For instance, the thermal increment caused by the manufacturing of the i^{th} layer is derived from Eq. 3 and 4 and writes for $t \leq t_i$:

$$T_i(x,z,t) = \int_{t'=0}^{t} dT_i(x,z,t) \text{ with } dT_i(x,z,t) = \frac{Q_i(t)}{2\pi ke} \exp\left[-\frac{\lambda\left((x-x_i')^2 + (z-z_i')^2\right)}{2(t-t')} - \frac{2h(t-t')}{ec\rho} \right] \frac{dt'}{t-t'} \tag{9}$$

Since the analytic model is linear, the superposition principle can be used to sum the contributions of all the real sources S_i and of all the fictitious sources attached to each S_i to model the edges. To ensure the continuity of the solution across the different layers, a diffusion mechanism is introduced when a new layer is built. This is performed using a Gaussian filter, which is similar to heat diffusion, since it is the solution of the heat equation in the absence of sources:

$$\mathcal{G}_\sigma.T\,(x,z,t) := \frac{1}{2\pi\sigma^2} \iint_{-\infty}^{+\infty} \exp\left(-\frac{\hat{x}^2 + \hat{z}^2}{2\sigma^2} \right) T(x-\hat{x}, z-\hat{z}, t)\, d\hat{x}d\hat{z} \tag{10}$$

The thermal fields exhibited in Fig. 3 illustrates the different steps of the numerical method:

(a) Considering that the thermal field during the printing of the i^{th} layer is known (Fig. 3a),

(b) Once the i^{th} layer is printed, the layer $i + 1^{\text{th}}$ appears at room temperature on top of the previous one (Fig. 3b);

(c) To avoid discontinuity of the thermal field between the layers, the heat accumulated during the printing of the first i layers is diffused in the new layer using a Gaussian filter with a characteristic distance equal to the layer thickness, $\sigma = \Delta z$ (Fig. 3c);

$$\tilde{T}_i(x,z,t) = \mathcal{G}_{\Delta z}.\sum_{j=1}^{i} T_j\,(x,z,t) \quad \text{where } T_j \text{ is defined according to Eq. 9} \tag{11}$$

(d) The thermal increment only due to the printing of the $i + 1^{\text{th}}$ layer is derived from the contribution of source S_{i+1}:

$$T_{i+1}(x,z,t) = \int_{t'=0}^{t} dT_{i+1}(x,z,t) \quad \text{with } dT_{i+1} \text{ derived from Eq. 9} \tag{12}$$

(e) The principle of superposition is applied to derive the complete thermal field by summing the thermal increments caused by the manufacturing of layer $i+1$ with the previous ones submitted to diffusion and the total thermal field during the printing of layer $i+1$ (Fig. 3e) writes:

$$T(x,z,t) = T_{i+1}(x,z,t) + \mathcal{G}_\sigma . \sum_{j=1}^{i} T_j\ (x,z,t) \tag{13}$$

3.5. Numerical implementation and computational time

The model described above was implemented in *Python 3* using *NumPy* and *SciPy* libraries [45]. The thermal field is evaluated on a regular two-dimensional spatial grid and numerical time integration is performed using the *integrate* package of *SciPy* library.

In Sect. 1 the advantage of this kind of model was stated: they offer short computational times. In particular, the computational time is proportional to the number of nodes where the temperature is evaluated. On a 2-core processor $2.30\,GHz$, deriving the temporal evolution at one position during 300 seconds (5 minutes) at 10 Hz takes 28 CPU-seconds and a thermal map of 100 x 100 nodes takes 29 CPU-seconds to compute.

These performances could be further improved by optimizing the code, switching for example from *Python* to *C/C++* programming language.

4. Results

This section contains a confrontation between the predictions of the model (see Sect. 3) and the experimental measurements (see Sect. 2).

The following test configurations will be considered:

- Experience (E1): 30-second dwell time, measurements on thermocouples T1 and T2;
- Experience (E2): 30-second dwell time, measurements on thermal camera;
- Experience (E3): no dwell time, measurements on thermocouples T1 and T2.

Let us remark that only experiments with dwell time respect the linearity assumption and can be reproduced by the present model. Therefore, (E1) will serve for the identification of parameters whereas data extracted from (E2) are dedicated to validation. (E3) will be used for comparison only, to highlight the importance of the thermal linearity assumption and illustrates the limits of the model.

4.1. Parameter identification from thermocouples measurements

Only two of the parameters of the model listed in Table 2 are not known accurately: the convection coefficient h and the absorptivity A.

The identification of these parameters was done on the data of (E1), i.e. on the thermal evolution monitored by the thermocouples T1 and T2 for the specimen with a 30-second dwell time. The best fit between experimental and predicted data was obtained for $h = 25\,W.m^{-2}.K^{-1}$ and $A = 0.35$.

These values were compared to literature data. In [11], Heigel *et al.* use a convection coefficient varying from 20 to 60 $W.m^{-2}.K^{-1}$. The range of absorptivity that can be found in the literature for SS316 is quite large depending on the wavelength of the laser. No information could be found for a fiber laser with a $1070\,nm$ wavelength but in [41], Debroy*et al.* gives an absorptivity between 0.25–0.32 for a Nd:YAG laser with wavelength $1060\,nm$. Therefore, this identification appears to be consistent with the literature.

The Fig. 4 displays the comparison of the thermocouples measurements and predicted temperature on the specimen manufactured on (E1) after the identification of the convection coefficient h and absorptivity A for thermocouples T1 and T2. The highly accurate fit testifies for the model quality. An important discrepancy is however observed for the temperature peaks at the beginning of the printing, this is certainly due to the thermocouples frequency acquisition. Indeed, the temporal derivative of temperature is very high due to the rapid motion of the laser and the localized heat input. Therefore, the acquisition frequency is certainly too low to capture the precise maximum temperature.

Let us further remark the two time scales of the time evolution:

(a) Thermal field during the printing of layer i.

(b) Apparition of layer $i+1$ at room temperature.

(c) Diffusing the heat from the first i layers.

(d) Thermal increment caused by the manufacturing of layer $i+1$.

(e) Total thermal field during the printing of layer $i+1$.

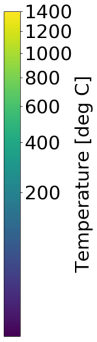

Figure 3: Internal steps of the algorithm developed to model the printing of successive layers: (a) printing of the i^{th} layer; (b) adding the $i{+}1^{\text{th}}$ layer at room temperature; (c) diffusing the heat of the previous layers in the new layer to avoid discontinuity of the thermal field (Eq. 11); (d) derivation of the contribution of source $i+1$ (Eq. 12); (e) superposition of thermal increments from all sources.

(i) a short one corresponding to the passage of the laser at each layer deposition, the location ($x = L/2, z = 0$) experiences a temperature rise each time the laser comes right over it, followed by a very fast cooling;

(ii) a longer one describing the fact that the part warms up during the process until it reaches an annealing temperature which in this case seems to be around 60°C for T1 and T2. However, for the location of thermocouple T1, the temperature peaks decrease while the laser goes on printing the above layers whereas for thermocouples T2 which 5mm below T1, the temperature peaks increase first as the first layers warms the component and finally decreases as the laser gets further.

Furthermore, the results show that the optimal choice of parameters permits to reconstruct the thermal evolution at two different locations. This indicates that the shape of semi-analytic solutions proposed here are suitable to model the thermal evolution during DED.

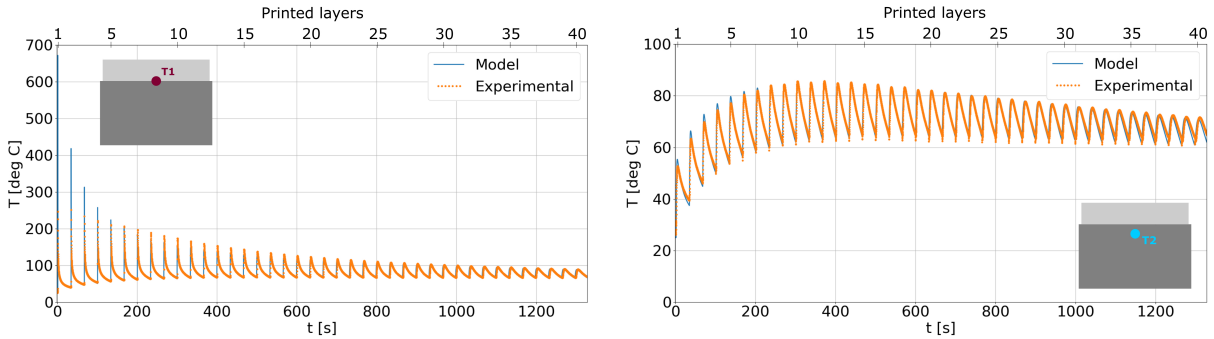

(a) Thermocouple T1.

(b) Thermocouple T2.

Figure 4: Comparison of the thermocouples measurements and predicted temperature on the specimen manufactured on (E1) (30-second dwell time) after the identification of the convection coefficient h and absorptivity A.

4.2. Model validation on thermal camera data

The aim of the validation process is to compare model prediction with the temperature field measured by the thermal camera in (E2) in terms of accuracy of: (i) spatial distribution at a certain time and (ii) time evolution at a given position.

The comparison between the thermal fields predicted by the model and the thermal measurements of the camera is displayed in Fig. 5, 6 and 7 at three different time instants. For each one, six figures are displayed: the predicted (a) and experimental (c) thermal maps with a magnification around the melt pool ((b) and (d)) which provides a qualitative comparisons; then, to enable a more quantitative analysis, the thermal variation along two lines, (e) horizontal $1\,mm$ below the top edge and (f) vertical $1\,mm$ behind the laser spot, is plotted for the model and the measurements.

The three moments are taken when the building of the wall is sufficiently advanced and the thermal fields can be accurately measured. They are all extracted from the printing of the 67^{th} layer (arbitrary choice), when the DED deposit is $13.4\,mm$. At moment t_1 displayed in Fig. 5, the nozzle is leaving the left edge; at instant t_2 (Fig. 6), the laser is in the middle of its path; at instant t_3 (Fig. 7), the source is close to the right edge. The proximity of the edges at the first and third moments will assess the ability of the model to take them into account.

The analysis of the graphs highlights that the model predicts warmer temperature near the melt pool than the experiments. In Sect. 3, it was stated that the material parameters was not varying with temperature to ensure the existence of an analytic solution. Phase change is also not accounted for in the present model which is another reason to expect a poor accuracy near the melt pool.

With the exception of the neighborhood of the melt pool, spatial distribution appears to be well captured for all the nozzle positions. The model is then able to capture the thermal gradient generated by a localized moving heat source even in the vicinity of adiabatic edges.

The thermal field acquired by the camera also provides the evolution of temperature of one pixel over time which corresponds to the temporal evolution of the temperature at one location. The graphs of Fig. 8 displays the curves temperature versus time at two different locations both for the model and the experiments. The locations observed were chosen far from the thermocouples position, at an arbitrary

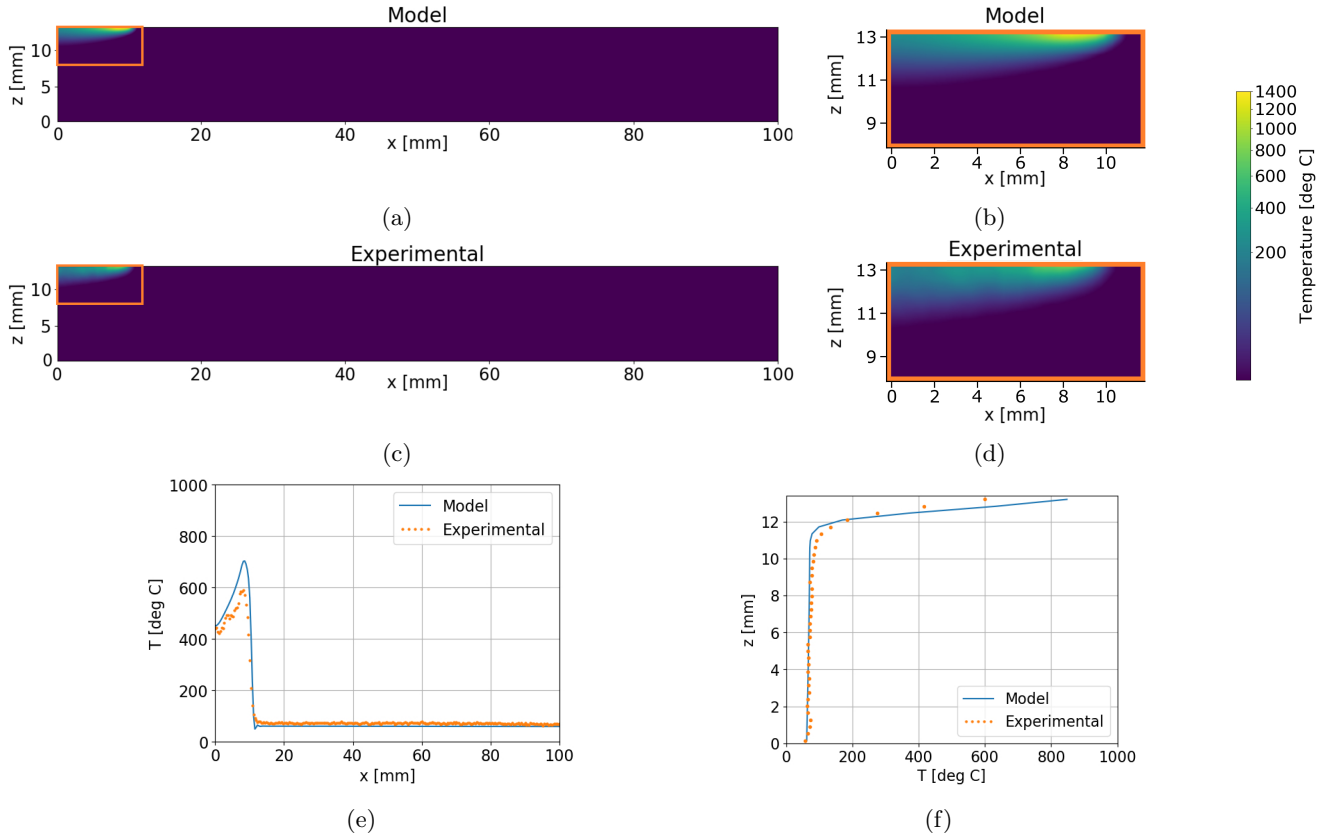

Figure 5: Comparison of the thermal field predicted by the model and the one measured by the camera during (E2) (30-second dwell time) at instant t_1. Predicted, respectively experimental, general thermal maps are displayed in (a), respectively (c) while (b) and (d) provide zoom on the melt pool region. (e) and (f) exhibit the thermal variation along horizontal line (1mm below the top edge) and vertical line (1mm below the laser spot).

height of 8.2 mm in the DED part. One is located in the middle of the laser path ($x = 50\,mm$) while the other is near the right edge ($x = 98\,mm$).

The misfit between the measured and predicted peak temperatures observed both on Fig. 8a and 8b can be explained by the following rationale. First, the low sampling rate of the camera does not capture the fast thermal evolution and actually misses the maximum temperature caused by one laser passage. Second, the model is not accurate when the material is in the liquid state because no phase change is modeled and consequently, the predicted peak temperature is uncertain.

Except from those peaks, the model fits very accurately the measured cooling rates, within the camera acquisition range, that is to say above 150 $°C$. For the point located in the middle of the laser path (Fig. 8a), model and experiments perfectly match. At the point located near the edge (Fig. 8b), the model seems less accurate. In particular, the cycles looks different for the model if the laser is going left or right whereas this is not observed in the experimental curve. So, it seems that the model emphasizes more the effect of bidirectional lasing strategy than the thermal measurements.

4.3. Limits of superposition principle

In this paragraph, the data collected on the specimen manufactured without dwell time during (E3) is used to insist on the necessity of applying the model to a case where the thermal field is linear.

In the absence of dwell time, the panel does not have enough time to cool down between two laser paths. Consequently, in this configuration, the superposition principle does not apply. The temperature evolution of Fig. 9 show that the model predictions overestimates strongly of temperature. This comparison is of great interest since it underlines one limit of the present semi-analytic thermal model and exhibits a case where it should not be used.

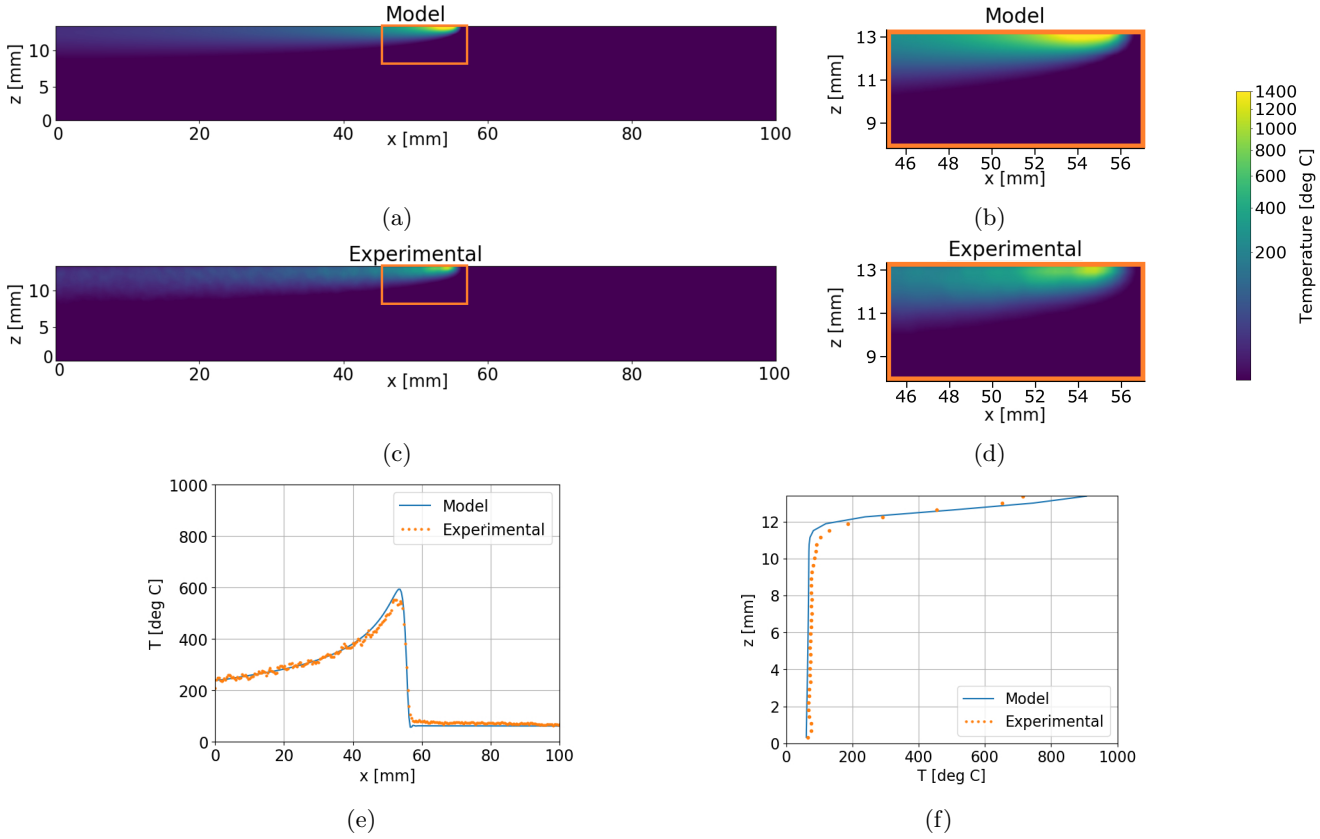

Figure 6: Comparison of the thermal field predicted by the model and the one measured by the camera during (E2) (30-second dwell time) at instant t_2. Predicted, respectively experimental, general thermal maps are displayed in (a), respectively (c) while (b) and (d) provide zoom on the melt pool region. (e) and (f) exhibit the thermal variation along horizontal line (1mm below the top edge) and vertical line (1mm below the laser spot).

4.4. Conclusions

It is important to notice that the calibration was made on the temporal evolution of temperature at 2 points, in the middle of the structure by fixing only two parameters. The validation part carried out with the thermal camera data has shown that the model predicts accurately both the spatial gradient at different moments and the thermal evolution in different locations, including near the edge.

Last but not least, the necessity of working on configurations where the non-linearity of heat equation can be neglected was demonstrated since the superposition principle is the key feature used to model the printing of several layers in a short computation time.

5. Discussion

This last section contains a discussion on the limitations, perspectives and possible applications of the semi-analytic model developed above.

5.1. Validity domain

In the proposed model, material parameters must be independent of temperature to ensure the analytic resolution of Eq. 2. This assumption of linearity authorize to apply the superposition principle to model the manufacturing of several layers. However, it has been observed in Sect. 4.3 that when no dwell time is applied, the non-linearity cannot be neglected and that the model fails to predict the thermal evolution measured by the thermocouples.

In [41], Debroy *et al.* recall polynomial expressions for 316L stainless steel material parameters:

$$\begin{array}{lcll} k(T) & = & A_1 + B_1 T & \text{with } A_1 = 11.82 \text{ and } B_1 = 0.0106 \\ c(T) & = & A_2 + B_2 T + C_2 T^2 + D_2 T^3 & \text{with } A_2 = 330.9, B_2 = 0.563, \\ & & & C_2 = -4.015 \times 10^{-4} \text{ and } D_2 = 9.465 \times 10^{-8} \end{array} \quad (14)$$

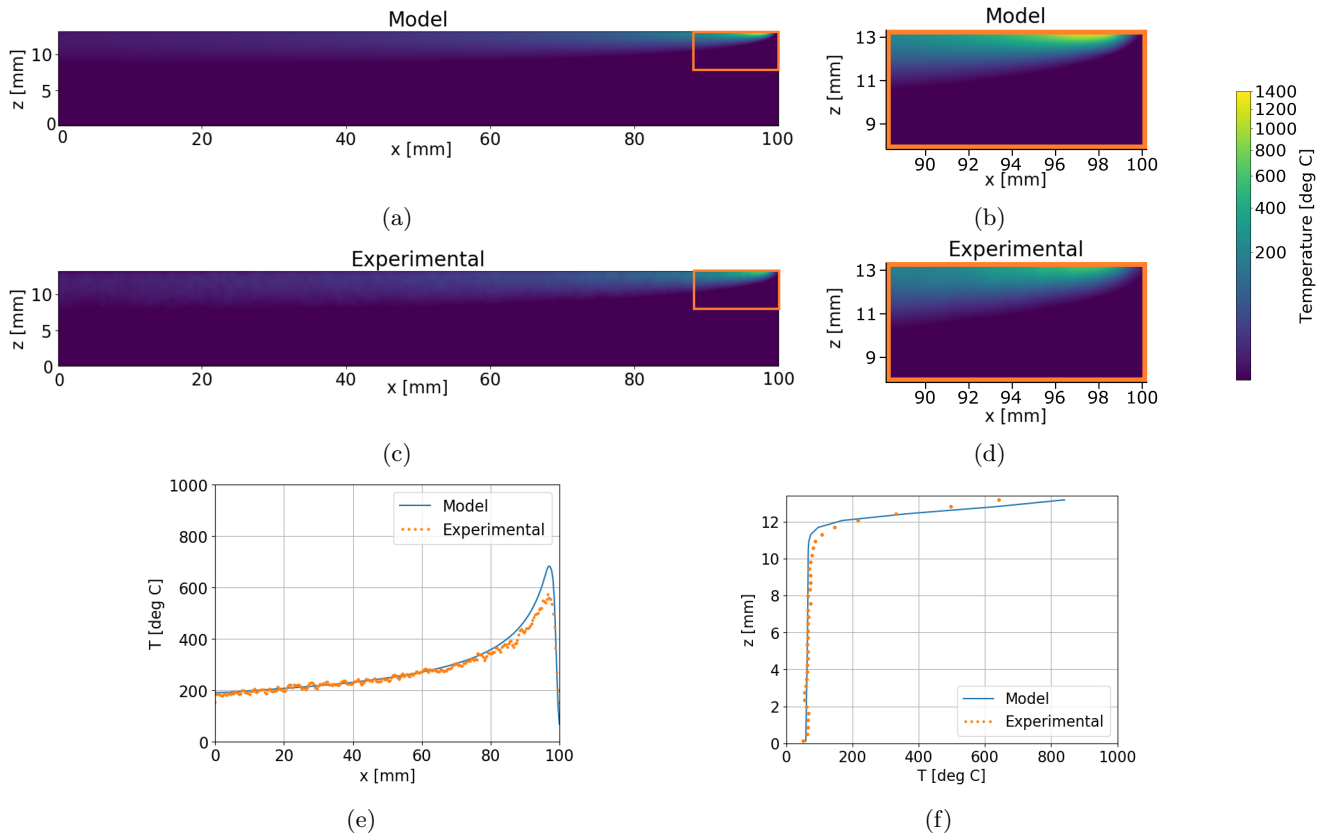

Figure 7: Comparison of the thermal field predicted by the model and the one measured by the camera during (E2) (30-second dwell time) at instant t_3. Predicted, respectively experimental, general thermal maps are displayed in (a), respectively (c) while (b) and (d) provide zoom on the melt pool region. (e) and (f) exhibit the thermal variation along horizontal line (1mm below the top edge) and vertical line (1mm below the laser spot).

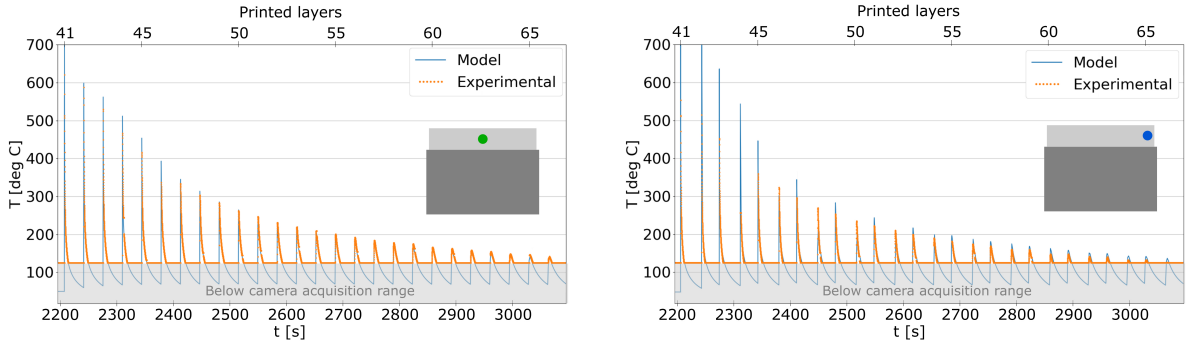

(a) Thermal evolution in the center of the wall at point ($x = 50\,mm, z = 8.2\,mm$).

(b) Thermal evolution near the right edge at point ($x = 98\,mm, z = 8.2\,mm$).

Figure 8: Comparison of the thermal evolution predicted by the model and the one measured by the thermal camera during (E2) (30-second dwell time) for two locations on the wall: (a) in the middle of the laser path and (b) near the right edge.

with T expressed in K, k in $W.m^{-1}.K^{-1}$ and c in $J.kg^{-1}.K^{-1}$. The corresponding evolution of k and c are displayed in Fig. 10a.

In order to know when the non-linearity is too important to be neglected, the following estimators

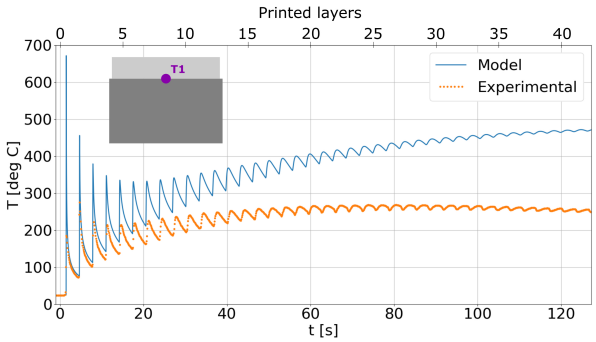

(a) Thermocouple T1, $x = 50$mm and $z = 0$mm.

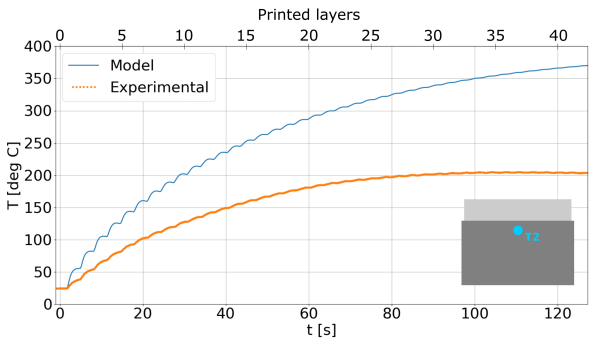

(b) Thermocouple T2, $x = 50$mm and $z = -5$mm.

Figure 9: Comparison of the thermocouples measurements and predicted temperature on the specimen manufactured on (E3) (no dwell time) highlighting the importance of the superposition principle.

are proposed:

$$\begin{aligned} e_k &= \frac{1}{V k(T_0)} \iiint_V |k(T_0) - k(T)| dV \\ e_c &= \frac{1}{V c(T_0)} \iiint_V |c(T_0) - c(T)| dV \end{aligned} \tag{15}$$

where $k(T)$ and $c(T)$ are derived from Eq. 14. T is the thermal field in the component just before the superposition principle is applied for the first time, ie at $t = L/v + t_{dwell}$. The graph of Fig. 10b displays that the non-linearity levels estimated by e_k and e_c for different dwell times. It appears that the two estimators of Eq. 15 are very close to each other and that they decrease with the addition of dwell time since the temperature in the component gets closer to the reference temperature T_0. The role played here by dwell time in the cooling of the structure could also be conducted by thermal pumping in more massive components.

Consequently, a rule of thumb could be deduced from the results of Fig. 10b: this model should only be used on configurations (geometry and process parameters) where the estimator of non-linearity e is below 5%. This threshold can be refined by conducting additional experimental measurements during manufacturing with intermediary dwell times.

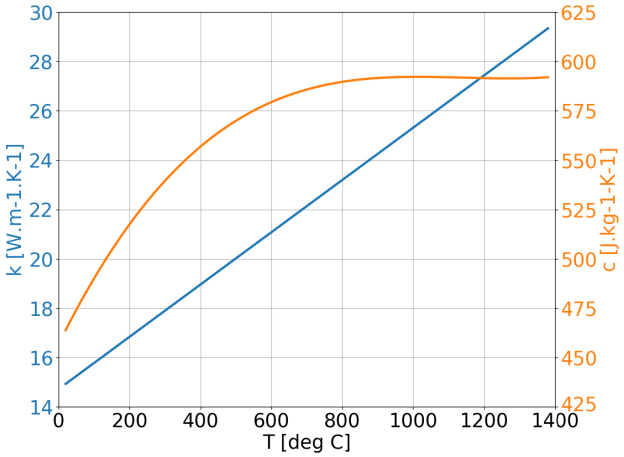

(a) Evolution of material parameters with temperature for 316L stainless steel [41].

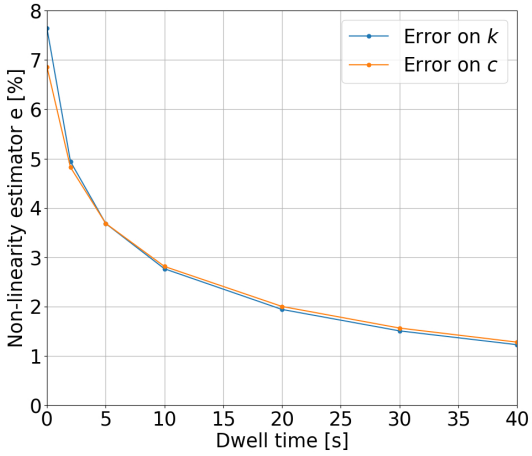

(b) Longer dwell time between two successive layers reduce the non-linearity estimator.

Figure 10: Non-linearity estimator: (a) the non-linearity of the thermal field comes from the variation of material parameters with temperature; (b) the error made by applying the superposition principle can be estimated with the non-linearity estimator of Eq. 15.

As a conclusion, the validity domain of the simplified approach presented here is the following : bi-dimensional geometry with small non-linearity (dwell time or thermal pumping). The absence of phase

change modeling also results in an error around the melt pool since no phase change and fluid convection are modeled. However, it was demonstrated in Sect. 4 that it is accurate in its validity domain and it is a useful tool which allows a fast exploration of process parameters thanks to its low computational cost.

5.2. Three-dimensional structures

The present study focuses on bi-dimensional structures since the application of interest is blade repair on geometries similar to those displayed in [36, 37]. However, similar work could be conducted on massive geometries using the three-dimensional Rosenthal's equation [22]. It describes the thermal increment in a semi-infinite solid $z \leq 0$ for a laser source moving at speed v along the x axis ($x' = vt'$) and located in the plane $y' = 0$, $z' = 0$:

$$T^{\text{3D}}_{\text{transient}}(x, y, z, t) = \int_{t'=0}^{t} \frac{\sqrt{2\lambda}\, Q}{4\pi^{3/2} k} \frac{dt'}{(t-t')^{3/2}} \, \mathrm{e}^{-\frac{\lambda}{2(t-t')}\left((x-vt')^2 + y^2 + z^2\right)} \tag{16}$$

Similarly to what was done in two dimension, from Eq. 16, the quasi-steady state can be derived by letting t goes to infinity, the temperature increment then becomes:

$$T^{\text{3D}}_{\text{quasi-steady}}(\xi, r) = \frac{Q}{2\pi k r} \, \mathrm{e}^{-\lambda v \xi} \, \frac{\mathrm{e}^{-\lambda v r}}{r} \tag{17}$$

where (ξ, r) are the relative coordinates when the reference frame is centered on the heat source ($\xi = x - vt$, $r = \sqrt{(x-vt)^2 + y^2 + z^2}$).

Edges can be modeled similarly by adding fictitious sources symmetrically to boundaries. Convection cannot be introduced as it was done for the bi-dimensional model, however on a massive geometry, this cooling mechanism can be neglected in front of conduction.

5.3. Determination of optimal dwell time

The experimental measurements of Fig. 4 and 9 exhibit the impact of dwell time on the annealing temperature. Without dwell time, the annealing temperature for T1 is close to 250°C whereas it was only 60°C with 30 seconds of dwell time. Similarly, it is 200°C without dwell time and 60°C with a 30-second dwell time for thermocouple T2. This major difference can result in different microstructures and consequently material properties or different residual stresses distribution as already observed in [10–12, 46].

Depending of the type of alloys used, it can be either desirable or not to maintain a high annealing temperature in the component and many aspects need to be taken into account (distortion, hot cracking, residual stress, metallurgical transformations). Foster *et al.* have for example shown in [46] that introducing a dwell time reduces the residual stresses in a DED Inconel 625 component.

Nevertheless, the introduction of dwell time has industrial consequences. To maintain a steady powder stream, the powder jet cannot be interrupted during the manufacturing by fear of generating an irregular material flow. Then, dwell time causes a consequent waste of powder and should be reduced to its minimum. The manufacturing process should also be kept as short as possible. Consequently, it is important to optimize the dwell time duration depending on material considerations.

Fig. 11 displays a graph showing the thermal evolution for thermocouple T1 for different dwell times. This enables a fast choice of the shortest dwell time that enables to reach the desired annealing temperature.

Without a fast process simulation tool, such an estimation of the optimal dwell time can be time-consuming whereas semi-analytic model can easily provide information taking into account the cooling of the component due to both conduction and convection.

5.4. Spatial thermal gradient and solidification maps

Thermal gradient and cooling rates are of major importance since the solidification condition affects the grain size and morphology so as the presence and type of dendrites forming. Solidification maps are commonly drawn in a G-R plane where G is the thermal gradient and R is the interface solid-liquid velocity. For example, the map shown in Fig. 13a shows a solidification map for SS 316 from [47] with a frontier between equiaxed grains and columnar grains. In two dimensions, the thermal gradient reads $G = \sqrt{\frac{\partial T}{\partial x}^2 + \frac{\partial T}{\partial z}^2}$. The interface velocity can be derived by dividing the cooling rate by the thermal gradient $R = \frac{\partial T}{\partial t} / G$, as explained by Gockel *et al.* in [30]. In order to be able to locate the manufacturing

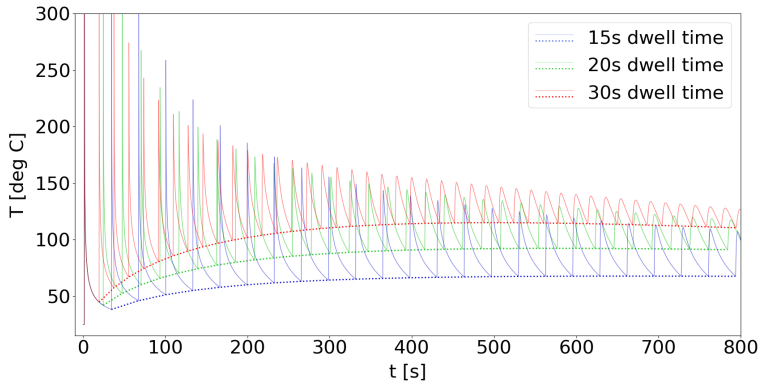

Figure 11: Influence of dwell time on annealing temperature. The thermal evolution at the position of thermocouple T2 is computed for three different dwell times : 15 seconds, 20 seconds and 30 seconds.

conditions in the map of Fig. 13a, G and R need to be estimated at the melt pool limit, i.e. on the melting temperature isotherm line.

The first option is to derive the cooling rates and the spatial thermal evolution using the analytic formulation for the quasi-steady state. Noting $\alpha = \sqrt{(\lambda v)^2 + \frac{2h}{ek}}$, the quasi-steady bi-dimensional Rosenthal's solution of Eq. 31 writes

$$T(x,z,t) = \frac{Q}{\pi k e}\, \mathrm{e}^{-\lambda v(x-vt)}\; K_0\left(\alpha\, \sqrt{(x-vt)^2+z^2}\right) \tag{18}$$

The following partial derivatives can be easily obtained:

$$\begin{aligned}
\frac{\partial T}{\partial t}(x,z,t) &= \frac{vQ}{\pi k e}\, \mathrm{e}^{-\lambda v(x-vt)} \left[\frac{\alpha(x-vt)}{\sqrt{(x-vt)^2+z^2}}\, K_1\left(\alpha\, \sqrt{(x-vt)^2+z^2}\right) + \lambda v\, K_0\left(\alpha\, \sqrt{(x-vt)^2+z^2}\right)\right] \\
\frac{\partial T}{\partial x}(x,z,t) &= -\frac{Q}{\pi k e}\, \mathrm{e}^{-\lambda v(x-vt)} \left[\frac{\alpha(x-vt)}{\sqrt{(x-vt)^2+z^2}}\, K_1\left(\alpha\, \sqrt{(x-vt)^2+z^2}\right) + \lambda v\, K_0\left(\alpha\, \sqrt{(x-vt)^2+z^2}\right)\right] \\
\frac{\partial T}{\partial z}(x,z,t) &= -\frac{Q}{\pi k e}\, \mathrm{e}^{-\lambda v(x-vt)} \frac{\alpha z}{\sqrt{(x-vt)^2+z^2}}\, K_1\left(\alpha\, \sqrt{(x-vt)^2+z^2}\right)
\end{aligned} \tag{19}$$

where K_1 is the modified Bessel function of the second kind, order 1 and is worth the opposite of the derivative of K_0, $K_0' = -K_1$ [48]. Gockel *et al.* show in [30] that this simple evaluation gives promising results in quasi-steady regime.

However, to account for the superposition of different sources and for the panel edges, the thermal gradient around the melt pool can be derived in the transient state, using finite difference. An overview of the typical temperature distribution and gradient is displayed in Fig. 12. Depending on the layer considered and the dwell time used to print the sample, the thermal gradient is estimated between $10^5 - 10^6$ K/m. This order of magnitude is confirmed by the work of Gockel *et al.* [30].

The numerical evaluation of R confirms that the melt pool follows the laser motion with a speed close to the nozzle speed, $R \simeq v = 2000\, mm/s = 3.3\, \mathrm{e}^{-2} m/s$. Once reported in the solidification map of Fig. 13a, the values of R and G gives a zone in the columnar region. This is consistant with Electron BackScatter Diffraction analyses conducted in the literature such as the one displayed in Fig. 13b, where columnar grains morphologically aligned with the direction of thermal gradient in each layer can be observed [34].

It is true that the Rosenthal's solution does not model accurately phenomena around the melt pool because material parameters do not depend on temperature and phase change is not modeled. However, as this diagram is drawn in a log-log plane, the error made by the model due to its simple assumptions will not affect drastically the position of the region drawn in the map.

Consequently, it can be assumed that despite all the approximations made by the model, it is possible to estimate the nature of the component microstructure using this simplified thermal model and solidification maps.

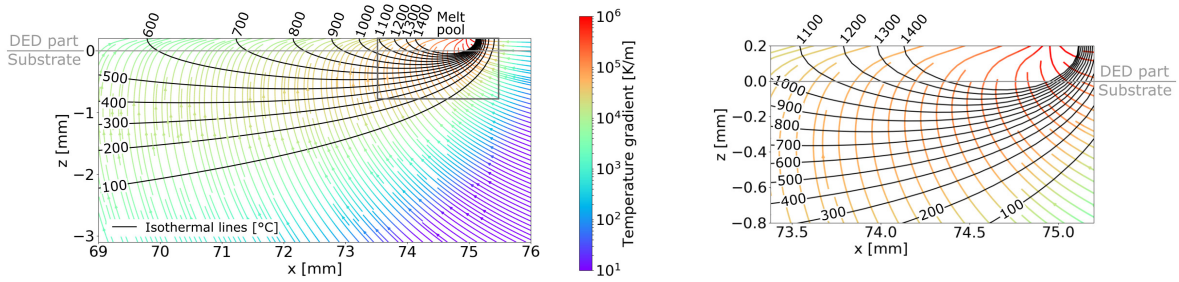

(a) (b)

Figure 12: Spatial thermal gradient in the repaired structure during the printing of the first layer : (a) general view and (b) zoom around the melt pool.

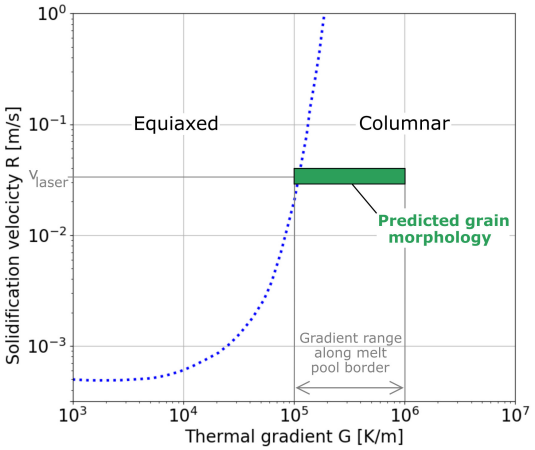

(a) Solidification map.

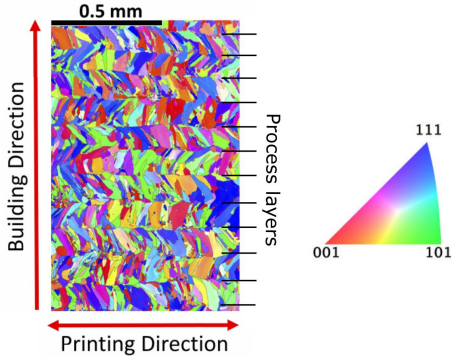

(b) Inverse Pole Figure along the building direction [34].

Figure 13: Predicting the grain morphology with solidification maps : (a) the solidification conditions for this study are located in the columnar region. The domain between equiaxed and columnar grains is extracted from [47]. This is consistent with results of the literature: (b) Inverse Pole Figure (IPF) along the building direction of a SS316 specimen manufactured with similar process parameters obtained by Electron BackScatter Diffraction [34].

6. Conclusion

The present study proposed a fast-computational model for temperature prediction during the repair of slender panels by DED. It is based on a semi-analytic approach and requires low computational times. The laser path is divided into infinitesimal heat sources and the thermal increment caused by each source is derived analytically, taking into account the convection at the surface of the wall. All those contributions are then summed by numerical integration allowing us to model the transient state of the process. The addition of layers is then conducted by superposing the heat sources and by diffusing of the heat of the previous layers in the current layer.

This model offers unprecedented advantages regarding the estimation of the thermal field during the whole additive manufacturing process in a short computation time. Indeed, the possibility to compute the temperature at any time, independently of previous temperature fields gives a great freedom and removes the problem of time step. Second, as the result is evaluated on a grid where the temperature at one point is independent from the temperature of neighboring points, there is no issue of mesh refinement. Finally, the computations are done in the transient state, enabling to take into account the influence of dwell time, edges and convection.

The comparison between experimental measurements and model predictions has highlighted that the accuracy of the model is good when the part cools down between the layers (long duration of one laser path or long dwell time, strong thermal pumping). However, due to the linearity assumption and the use of superposition principle, it strongly overestimates the temperature when the manufacturing consists of a rapid concatenation of laser path. The validity of the domain is nevertheless not too restrictive and this model can be used for many industrial problems focusing on quality and repeatability of laser paths.

Within its validity domain, it allows to study both spatial thermal gradient and temporal evolution which are of capital importance for final microstructure and mechanical properties. It enables the determination of the minimum dwell time to apply between two successive layers in order to deposit each layer on a cold component or the prediction of solidification conditions and grain morphology on the final component.

Several perspectives can be considered for this work. First, the model could be extended to other geometries and to three dimensions where the Rosenthal's solutions can also be derived. Experimental validations on other geometries or with different process parameters (particularly intermediary dwell times) could be carried out in order to get a better knowledge of the model validity domain.

Acknowledgment

The authors would like to thank *Direction Général de l'Armement* (DGA) for the funding of the *BeAM Mobile* DED machine used in this study.

[1] Pavel Hanzl, Miroslav Zetek, Tomas Baksa, and Tomas Kroupa. The influence of processing parameters on the mechanical properties of SLM parts. *Procedia Engineering*, 100:1405 – 1413, 2015. 25th DAAAM International Symposium on Intelligent Manufacturing and Automation, 2014.

[2] V. Ocelik, I. Furar, and J.Th.M. De Hosson. Microstructure and properties of laser clad coatings studied by orientation imaging microscopy. *Acta Materialia*, 58(20):6763 – 6772, 2010.

[3] Lakshmi L. Parimi, Ravi G. A., Daniel Clark, and Moataz M. Attallah. Microstructural and texture development in direct laser fabricated Inconel 718. *Materials Characterization*, 89:102 – 111, 2014.

[4] Zhuqing Wang, Todd A. Palmer, and Allison M. Beese. Effect of processing parameters on microstructure and tensile properties of austenitic stainless steel 304L made by directed energy deposition additive manufacturing. *Acta Materialia*, 110:226 – 235, 2016.

[5] Kangbo Yuan, Weiguo Guo, Penghui Li, Jianjun Wang, Yu Su, Xin Lin, and Yanping Li. Influence of process parameters and heat treatments on the microstructures and dynamic mechanical behaviors of Inconel 718 superalloy manufactured by laser metal deposition. *Materials Science and Engineering: A*, 721:215 – 225, 2018.

[6] Haider Ali, Hassan Ghadbeigi, and Kamran Mumtaz. Effect of scanning strategies on residual stress and mechanical properties of selective laser melted ti6al4v. *Materials Science and Engineering: A*, 712:175 – 187, 2018.

[7] Carolin Korner, Harald Helmer, Andreas Bauereiß, and Robert Singer. Tailoring the grain structure of IN718 during selective electron beam melting. *MATEC Web of Conferences*, 14:08001, 01 2014.

[8] Bonny Onuike and Amit Bandyopadhyay. Additive manufacturing in repair: Influence of processing parameters on properties of inconel 718. *Materials Letters*, 252:256 – 259, 2019.

[9] H. L. Wei, J. Mazumder, and T. DebRoy. Evolution of solidification texture during additive manufacturing. *Nature*, 2015.

[10] Erik R. Denlinger, Jarred C. Heigel, Pan Michaleris, and T.A. Palmer. Effect of inter-layer dwell time on distortion and residual stress in additive manufacturing of titanium and nickel alloys. *Journal of Materials Processing Technology*, 215:123 – 131, 2015.

[11] J.C. Heigel, P. Michaleris, and E.W. Reutzel. Thermo-mechanical model development and validation of directed energy deposition additive manufacturing of Ti–6Al–4V. *Additive Manufacturing*, 5:9 – 19, 2015.

[12] Nathan A. Kistler, David J. Corbin, Abdalla R. Nassar, Edward W. Reutzel, and Allison M. Beese. Effect of processing conditions on the microstructure, porosity, and mechanical properties of Ti-6Al-4V repair fabricated by directed energy deposition. *Journal of Materials Processing Technology*, 264:172 – 181, 2019.

[13] Zhaorui Yan, Weiwei Liu, Zijue Tang, Xuyang Liu, Nan Zhang, Mingzheng Li, and Hongchao Zhang. Review on thermal analysis in laser-based additive manufacturing. *Optics & Laser Technology*, 106:427 – 441, 2018.

[14] Tien T. Roehling, Sheldon S.Q. Wu, Saad A. Khairallah, John D. Roehling, S. Stefan Soezeri, Michael F. Crumb, and Manyalibo J. Matthews. Modulating laser intensity profile ellipticity for microstructural control during metal additive manufacturing. *Acta Materialia*, 128:197 – 206, 2017.

[15] Hongze Wang and Yu Zou. Microscale interaction between laser and metal powder in powder-bed additive manufacturing: Conduction mode versus keyhole mode. *International Journal of Heat and Mass Transfer*, 142:118473, 2019.

[16] Zhengtao Gan, Hao Liu, Shaoxia Li, Xiuli He, and Gang Yu. Modeling of thermal behavior and mass transport in multi-layer laser additive manufacturing of ni-based alloy on cast iron. *International Journal of Heat and Mass Transfer*, 111:709 – 722, 2017.

[17] Patrice Peyre, Morgan Dal, S Ebastien Pouzet, and Olivier Castelnau. Simplified numerical model for the laser metal deposition additive manufacturing process. *Journal of Laser Applications, 29 (2)*, 2017.

[18] Guillaume Marion, Georges Cailletaud, Christophe Colin, and Matthieu Mazière. A finite element model for the simulation of direct metal deposition. *Conference Paper*, 10 2014.

[19] Daniel Weisz-Patrault. Fast simulation of temperature and phase transitions in directed energy deposition additive manufacturing. *Additive Manufacturing*, 31:100990, January 2020.

[20] D.W.M. Veldman, R.H.B. Fey, H.J. Zwart, M.M.J. van de Wal, J.D.B.J. van den Boom, and H. Nijmeijer. Semi-analytic approximation of the temperature field resulting from moving heat loads. *International Journal of Heat and Mass Transfer*, 122:128 – 137, 2018.

[21] Carslaw. *Introduction to the Mathematical Theory of the Conduction of Heat in Solids*, chapter 9, page 150. , 1921.

[22] Daniel Rosenthal. The theory of moving sources of heat and its application to metal treatments. *Transaction of the American Society of Mechanical Engineers*, 1946.

[23] T. W. Eagar and N. S. Tsai. Temperature fields produced by traveling distributed heat sources. *Welding Research supplement*, pages 346–355, 1983.
[24] John Goldak, Aditya Chakravarti, and Malcolm Bibby. A new finite element model for welding heat sources. *Metallurgical Transactions B*, 1983.
[25] John A Goldak. *Computational Welding Mechanics*. Springer, 2005.
[26] R. Komanduri and Z. B. Hou. Thermal analysis of the arc welding process: Part i. general solutions. *Metallurgical and Materials Transactions B*, 31(6):1353–1370, Dec 2000.
[27] Karin Heller, Steffen Kessler, Friedhelm Dorsch, Peter Berger, and Thomas Graf. Analytical description of the surface temperature for the characterization of laser welding processes. *International Journal of Heat and Mass Transfer*, 106:958 – 969, 2017.
[28] Guy Murry. Soudage et soudabilité métallurgique des métaux. *Techniques de l'ingénieur*, 1994.
[29] M. Van Elsen, M. Baelmans, P. Mercelis, and J.-P. Kruth. Solutions for modelling moving heat sources in a semi-infinite medium and applications to laser material processing. *International Journal of Heat and Mass Transfer*, 50(23):4872 – 4882, 2007.
[30] Joy Gockel, Nathan Klingbeil, and Srikanth Bontha. A closed-form solution for the effect of free edges on melt pool geometry and solidification microstructure in additive manufacturing of thin-wall geometries. *Metallurgical and Materials Transactions B*, 47(2):1400–1408, Apr 2016.
[31] Patcharapit Promoppatum, Shi-Chune Yao, P. Chris Pistorius, and Anthony D. Rollett. A comprehensive comparison of the analytical and numerical prediction of the thermal history and solidification microstructure of inconel 718 products made by laser powder-bed fusion. *Engineering*, 3(5):685 – 694, 2017.
[32] Y. Yang, M.F. Knol, F. van Keulen, and C. Ayas. A semi-analytical thermal modelling approach for selective laser melting. *Additive Manufacturing*, 21:284 – 297, 2018.
[33] Ryszard Parkitny and Jerzy Winczek. Analytical solution of temporary temperature field in half-infinite body caused by moving tilted volumetric heat source. *International Journal of Heat and Mass Transfer*, 60:469 – 479, 2013.
[34] Yanis Balit, Eric Charkaluk, and Andrei Constantinescu. Digital image correlation for microstructural analysis of deformation pattern in additively manufactured 316l thin walls. *Additive Manufacturing*, 31:100862, January 2019.
[35] Camille Guévenoux, Simon Hallais, Yanis Balit, Alexandre Charles, Eric Charkaluk, and Andrei Constantinescu. Plastic strain localization induced by microstructural gradient in laser cladding repaired structures. *Theoretical and Applied Fracture Mechanics*, 107:102520, June 2020.
[36] Guijun Bi and Andres Gasser. Restoration of nickel-base turbine blade knife-edges with controlled laser aided additive manufacturing. *Physics Procedia*, 12:402 – 409, 2011. Lasers in Manufacturing 2011 - Proceedings of the Sixth International WLT Conference on Lasers in Manufacturing.
[37] X. Penaranda, S. Moralejo, A. Lamikiz, and J. Figueras. An adaptive laser cladding methodology for blade tip repair. *The International Journal of Advanced Manufacturing Technology*, 92(9):4337–4343, October 2017.
[38] Oerlikon. Am metal powders. `https://www.oerlikon.com/am/en/offerings/metal-powders/`, 2019.
[39] BeAM. Gamme de machines - mobile et modulo. `http://www.beam-machines.fr/fr/produits`, 2016.
[40] Wikipedia. Thermocouples of type k. `https://en.wikipedia.org/wiki/Thermocouple#Type_K`, 2019.
[41] T. DebRoy, H.L. Wei, J.S. Zuback, T. Mukherjee, J.W. Elmer, J.O. Milewski, A.M. Beese, A. Wilson-Heid, A. De, and W. Zhang. Additive manufacturing of metallic components – process, structure and properties. *Progress in Materials Science*, 92:112 – 224, 2018.
[42] Optris. Xi 400 - technical data. https://www.optris.com/downloads-accessories-infrared-cameras, 2015.
[43] Azo Materials. Stainless steels - stainless 316 properties, fabrication and applications. `https://www.azom.com/`, 2019.
[44] Hua Tan, Jing Chen, Fengying Zhang, Xin Lin, and Weidong Huang. Process analysis for laser solid forming of thin-wall structure. *International Journal of Machine Tools and Manufacture*, 50(1):1 – 8, 2010.
[45] Scipy documentation. `https://www.scipy.org/docs.html`.
[46] B. K. Foster, A. M. Beese, J. S. Keist, E. T. McHale, and T. A. Palmer. Impact of interlayer dwell time on microstructure and mechanical properties of nickel and titanium alloys. *Metallurgical and Materials Transactions A*, 48(9):4411–4422, Sep 2017.
[47] Kai Zhang, Shijie Wang, Weijun Liu, and Xiaofeng Shang. Characterization of stainless steel parts by laser metal deposition shaping. *Materials & Design*, 55:104 – 119, 2014.
[48] Nico M. Temme. *Bessel Functions*, pages 235, formule 9.41. John Wiley & Sons, Inc., Hoboken, NJ, USA, 2011.

7. Appendices

7.1. Appendix 1: Fast integration model of the transient heat equation

The original transient solution proposed in two dimensions by Rosenthal in [22] does not account for thermal loss. First the way this solution is derived will be recalled. Then, a modification of the previous solution is proposed to take into account the convection along the two main edges of the panel $y = 0$ and $y = e$.

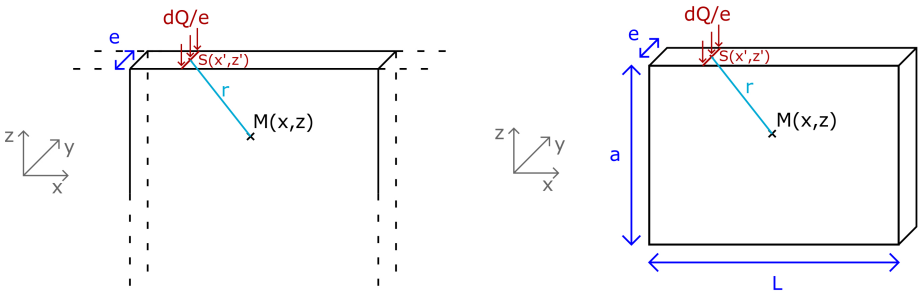

(a) Semi-infinite panel. (b) Panel with edges.

Figure 14: Panels of thickness e receiving an instantaneous linear power dQ/e on their top edge.

In [22], Rosenthal stated that, in adiabatic conditions, the thermal increment due to a linear heat source located at point (x', z') delivering an instanteneous power dQ/e at instant t' should satisfy the following system:

$$\text{Problem } \mathcal{P}_a : \begin{cases} \dfrac{\partial^2 T_a}{\partial x^2} + \dfrac{\partial^2 T_a}{\partial z^2} - 2\lambda \dfrac{\partial T_a}{\partial t} & = & 0, \\ T_a & \xrightarrow{t \to 0} & 0 \ , \quad r > 0, \\ T_a & \xrightarrow{r \to \infty} & 0, \\ -\displaystyle\int_{t'}^{t_0} \dfrac{\partial T_a}{\partial r}\, \pi r\, k\, dt & \xrightarrow[t_0 \to t']{r \to 0} & \dfrac{dQ}{e}, \end{cases} \tag{20}$$

where $r = \sqrt{(x - x')^2 + (z - z')^2}$ is the distance of a current point (x, z) to the heat source. This adiabatic problem $\mathcal{P}_a$ is composed of the heat equation in 2D and of boundary conditions. The last boundary condition is derived from the flux balance through a half-circle centered around the source; making this circle going to a point, the flux should give the power delivered by the source.

When the material parameters are assumed to be independent of temperature, Carslaw offered in [21] an analytic solution to the problem $\mathcal{P}_a$ for $t > t'$. This solution is actually the heat kernel, or Green's function, in two dimensions which writes:

$$dT_a(x, z, t) = \frac{dQ}{2\pi k e} \, \frac{1}{t - t'} \, \exp\left[-\frac{\lambda \left((x - x')^2 + (z - z')^2 \right)}{2(t - t')} \right]. \tag{21}$$

To describe a moving heat source along the x axis, Rosenthal introduces in [22] the relative coordinates in the reference frame centered on the heat source ($\xi = x - x', \zeta = z - z'$). In the case of a laser going along the x axis at constant speed v, delivering a constant instantaneous linear power $dQ = Q dt'$, $x' = vt'$ and $\xi = x - vt'$ so that

$$dT_a(x, z, t) = \frac{Q}{2\pi k e} \exp\left[-\frac{\lambda \left(\xi^2 + \zeta^2 \right)}{2(t - t')} \right] \frac{dt'}{t - t'} = \frac{Q}{2\pi k e} \exp\left[-\frac{\lambda \left((x - vt')^2 + (z - z')^2 \right)}{2(t - t')} \right] \frac{dt'}{t - t'} \tag{22}$$

In order to get the total time increment for one laser path in adiabatic conditions, one only needs to sum all the infinitesimal contributions of Eq. 22

$$T_a(x, z, t) = \int_{t'=0}^{t} dT_a(x, z, t) \tag{23}$$

For a slender panel, convection generates important thermal loss. Writing h the convection coefficient between the material and air, the energy balance on a volume element occupying the panel thickness submitted to a thermal increment T and to convection on the faces $y = 0$ and $y = e$ can be derived as

$$edxdz\ c\rho\ \left(\frac{\partial T}{\partial t}\right)_c + 2dxdz\ h\ T = 0 \tag{24}$$

and the thermal loss caused by convection consequently reads

$$\left(\frac{\partial T}{\partial t}\right)_c = -\frac{2h}{ec\rho}T. \tag{25}$$

By injecting Eq. 25 in the first line of Eq. 20, a new system satisfied by the temperature field in the presence of convection can be derived, it is denoted $\mathcal{P}_c$.

$$\text{Problem } \mathcal{P}_c : \begin{cases} \dfrac{\partial^2 T_c}{\partial x^2} + \dfrac{\partial^2 T_c}{\partial z^2} - 2\lambda\dfrac{\partial T_c}{\partial t} & = & \dfrac{2h}{ek}\ T_c, \\ T_c & \xrightarrow{t\to 0} & 0\ , \quad r > 0, \\ T_c & \xrightarrow{r\to\infty} & 0, \\ -\displaystyle\int_0^{t_0} \dfrac{\partial T_c}{\partial r}\ \pi r\ k\ dt & \xrightarrow[t_0\to 0]{r\to 0} & \dfrac{dQ}{e}, \end{cases} \tag{26}$$

This problem can also be solved analytically and its solution is:

$$dT_c(x,z,t) = \frac{dQ}{2\pi ke}\ \frac{1}{t-t'}\ \exp\left[-\frac{\lambda\left((x-x')^2+(z-z')^2\right)}{2(t-t')} - \frac{2h(t-t')}{ec\rho}\right] \tag{27}$$

Similarly to what was done for the adiabatic panel was taken into account, the solution where $x' = vt'$ and $dQ = Qdt'$ describes a laser path at constant speed and power:

$$dT_c(x,z,t) = \frac{Q}{2\pi ke}\ \exp\left[-\frac{\lambda\left((x-vt')^2+(z-z')^2\right)}{2(t-t')} - \frac{2h(t-t')}{ec\rho}\right]\ \frac{dt'}{t-t'} \tag{28}$$

Finally, the total thermal increment for one laser path taking into account convection is derived by integration of the infinitesimal contributions of Eq. 28:

$$T_c(x,z,t) = \int_{t'=0}^{t} dT_c(x,z,t) \tag{29}$$

Radiation losses also take part in thermal losses, it can be described by a radiative surface flux:

$$\phi_{\mathrm{r}} = \sigma\epsilon(T+T_0)^4 \tag{30}$$

where ϵ is the material emissivity, σ Stefan-Boltzmann constant and $T + T_0$ the absolute temperature given in Kelvin. As the radiative flux does not depend linearly on temperature, it was not possible to integrate it in the model as it was done for convection. Nevertheless, as this flux evolves in T^4, it will be high where the temperature is high that is to say near the melt pool. It is then assumed that radiations can be taken into account by lowering the structure absorptivity A of the laser power P, considering that only $Q = AP$ is actually going into the component.

One can show than when time goes to infinity, the transient solution proposed in Eq. 29 meets the quasi-steady Rosenthal's solution with convection (cf full demonstration in appendix 7.2):

$$T_c(x,z,t\to+\infty) = \int_{t'=0}^{+\infty} dT_c(x,z,t) = \frac{Q}{\pi ke}\ \mathrm{e}^{-\lambda v\xi}\ K_0\left(\sqrt{(\lambda v)^2 + \frac{2h}{ek}}\ r\right) \tag{31}$$

where (ξ, z) are the relative coordinates when the reference frame is centered on the heat source ($\xi = x - vt$, $r = \sqrt{\xi^2 + z^2}$) and K_0 stands for the modified Bessel function of the second kind order 0.

7.2. Appendix 2: From transient to steady solution

This appendix contains the demonstration showing how the transient solution matches the steady Rosenthal's solution with convection given in [22] for an infinite panel. Starting from the transient solution of Eq. 29, the steady solution corresponds to the case where the integration goes from 0 to an infinite time.

$$T(x,z,t) = \int_0^{+\infty} \frac{Q}{2\pi ke}\,\frac{dt'}{t-t'}\,\exp\left(-\frac{\lambda\left((x-vt')^2+z^2\right)}{2(t-t')}-\frac{2h}{ec\rho}(t-t')\right)$$

$$T(x,z,t) = \frac{Q}{2\pi ke}\int_0^{+\infty} \frac{dt'}{t-t'}\,\exp\left(-\frac{\lambda\left((x-vt+vt-vt')^2+z^2\right)}{2(t-t')}-\frac{2h}{ec\rho}(t-t')\right)$$

Change of variables: $\tau = t-t'$ and $\xi = x-vt$

$$T(\xi,z) = \frac{Q}{2\pi ke}\int_0^{+\infty} \frac{d\tau}{\tau}\,\exp\left(-\frac{\lambda\left((\xi+v\tau)^2+z^2\right)}{2\tau}-\frac{2h\tau}{ec\rho}\right)$$

$$T(\xi,z) = \frac{Q}{2\pi ke}\int_0^{+\infty} \frac{d\tau}{\tau}\,\exp\left(-\frac{\lambda\left(\xi^2+2v\tau\xi+v^2\tau^2+z^2\right)}{2\tau}-\frac{2h\tau}{ec\rho}\right)$$

$$T(\xi,z) = \frac{Q}{2\pi ke}\int_0^{+\infty} \frac{d\tau}{\tau}\,\exp\left(-\frac{\lambda(\xi^2+z^2)}{2\tau}-\lambda v\xi-\frac{\lambda v^2\tau}{2}-\frac{2h\tau}{ec\rho}\right)$$

Change of variable: $r = \sqrt{\xi^2+z^2}$

$$T(\xi,r) = \frac{Q}{2\pi ke}\,\mathrm{e}^{-\lambda v\xi}\int_0^{+\infty} \frac{d\tau}{\tau}\,\exp\left(-\frac{\lambda r^2}{2\tau}-\frac{\lambda v^2\tau}{2}-\frac{2h\tau}{ec\rho}\right)$$

Change of variables: $u = \frac{\tau\alpha}{\lambda r}$ where $\alpha = \sqrt{(\lambda v)^2+\frac{2h}{ek}}$

Using $c\rho = 2\lambda k$,

$$T(\xi,r) = \frac{Q}{2\pi ke}\,\mathrm{e}^{-\lambda v\xi}\int_0^{+\infty} \frac{du}{u}\,\exp\left(-\frac{r\alpha}{2u}-\frac{\lambda^2v^2ur}{2\alpha}-\frac{hur}{ek\alpha}\right)$$

$$T(\xi,r) = \frac{Q}{2\pi ke}\,\mathrm{e}^{-\lambda v\xi}\int_0^{+\infty} \frac{du}{u}\,\exp\left(-\frac{r\alpha}{2u}-\frac{ur}{2\alpha}\left(\lambda^2v^2+\frac{2h}{ek}\right)\right)$$

$$T(\xi,r) = \frac{Q}{2\pi ke}\,\mathrm{e}^{-\lambda v\xi}\int_0^{+\infty} \frac{du}{u}\,\exp\left(-\frac{r\alpha}{2u}-\frac{ur\alpha}{2}\right)$$

$$T(\xi,r) = \frac{Q}{2\pi ke}\,\mathrm{e}^{-\lambda v\xi}\int_0^{+\infty} \frac{du}{u}\,\exp\left(-\frac{r\alpha}{2}(u+\frac{1}{u})\right)$$

$$T(\xi,r) = \frac{Q}{2\pi ke}\,\mathrm{e}^{-\lambda v\xi}\;2K_0(\alpha r)\quad\text{from [48]}$$

$$\text{Hence}\quad T(\xi,r) = \frac{Q}{\pi ke}\,\mathrm{e}^{-\lambda v\xi}\;K_0\left(\sqrt{(\lambda v)^2+\frac{2h}{ek}}\;r\right)$$

7.3. Appendix 3: Position of fictitious sources

This section contains additional details about the modeling of the panel edges mentioned in Sect. 3.2.

Top and bottom edges.
Let us first start describing how the top and bottom edges are modeled by adding fictitious sources to make the planes $z = 0$ and $z = -a$ planes of symmetry. For a real source S_0 located at $(x', z' = 0)$ at t', an infinite number of fictitious sources S_n located at $(x', z' = 2na)$ with $n \in \mathbb{Z}^*$ are added to the model and the temperature increment is given by the superposition of the contributions of the real and fictitious sources:

$$dT(x, z, t, z' = 0, t') = \sum_{n\in\mathbb{Z}} dT^n(x, z, t, z' = 2na, t') \tag{32}$$

One can notice that only the contributions of the sources that are near the structure will have a first-order influence, since

$$\frac{dT^0}{dT^n} = \mathrm{e}^{\dfrac{\lambda na}{t-t'}(z-na)}. \tag{33}$$

Inded, using the inequality $-a \leq z \leq 0$, it is possible to show that

$$\begin{array}{lccccc} \text{for } n > 0, & \dfrac{dT^0}{dT^n} & \geq & \mathrm{e}^{\dfrac{n^2a^2\lambda}{t-t'}} & \geq & \mathrm{e}^{\dfrac{n^2a^2\lambda}{t}} \\ \text{and for } n < 0, & \dfrac{dT^0}{dT^n} & \geq & \mathrm{e}^{\dfrac{n(n+1)a^2\lambda}{t-t'}} & \geq & \mathrm{e}^{\dfrac{n(n+1)a^2\lambda}{t}}. \end{array} \tag{34}$$

Consequently, to decrease computational time, it is possible, at the first order, to limit the sum of Eq. 32 only to small values of $|n|$, $n = -1,\ 0$ or 1 in this study as it is shown in Fig. 15.

Left and right edges.
Similarly, the method of fictitious sources is used to model the edges $x = 0$ and $x = L$ and only the sources close to the structure will bring a thermal increment to the structure at the first order.

Indeed, one can show that, for a real source located at $x'_0 = \frac{L}{2}$ and fictitious sources located at $x'_m = \frac{L}{2} + mL$ with $m \in \mathbb{Z}$,

$$\frac{dT^0}{dT^m} = \mathrm{e}^{\dfrac{\lambda mL}{t-t'}(2x-(m+1)L)}. \tag{35}$$

Since $0 \leq x \leq L$,

$$n \in \mathbb{Z},\ \frac{dT^0}{dT^n} \geq \mathrm{e}^{\dfrac{m(m+1)L^2\lambda}{t}}. \tag{36}$$

For large m, the thermal increment is negligible and only contributions of sources $m = -1,\ 0$ or 1 will be considered in this study. The relative coordinates of a current point $M(x, z)$ in frames centered on fictitious sources need to be derived. For a laser path a constant speed v, $\xi_0 = x - vt'$. With the scheme of Fig. 15 illustrating the motion of eight fictitious sources considered, it is easy to read that for $m = -1$, $\xi_{-1} = x + vt$ and that for $m = 1$, $\xi_1 = 2L - x - vt$.

In Sect. 7.1, the way convection is taken into account along the edges $y = 0$ and $y = e$ of a semi-infinite panel is explained. The method of fictitious sources is used to model the effect of edges on conduction but nothing was said about convection on the surface of edges $x = 0$, $x = L$, $z = -a$ and $z = 0$. The convective flux through those surfaces being proportional to their area, the thermal loss on those edges is much smaller than the one on the edges $y = 0$ and $y = e$ since $e \ll a$ and $e \ll L$ and consequently it will be neglected.

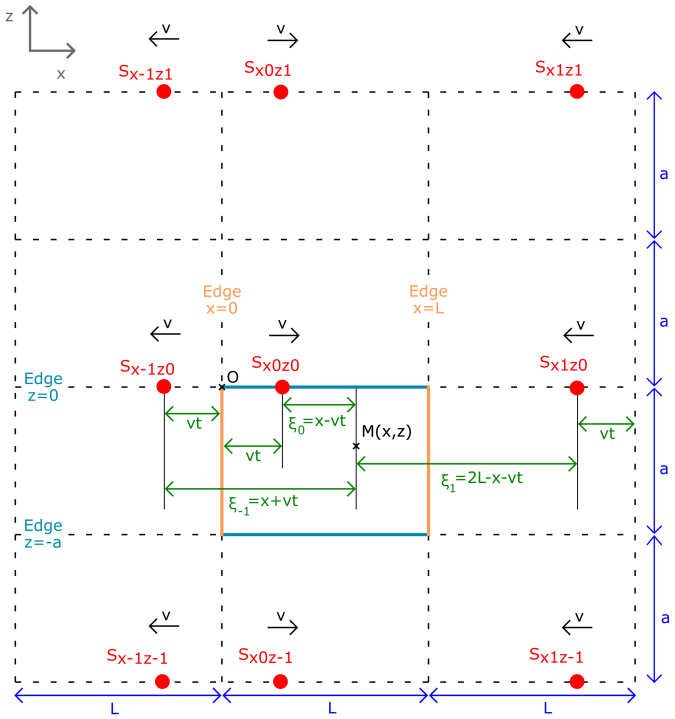

Figure 15: Fictitious sources used to model the panel edges: an adiabatic edge is equivalent to a plane symmetry.